

Fast-field-cycling, ultralow-field nuclear magnetic relaxation dispersion

Sven Bodenstedt,¹ Morgan W. Mitchell,^{1,2} and Michael C. D. Taylor^{1, a)}

¹ICFO – Institut de Ciències Fotòniques, The Barcelona Institute of Science and Technology, 08860 Castelldefels (Barcelona), Spain

²ICREA – Institució Catalana de Recerca i Estudis Avançats, 08010 Barcelona, Spain

(Dated: November 25th, 2020)

KEYWORDS

Molecular motion; Ultralow-field nuclear magnetic resonance (ULF NMR); Optically pumped magnetometers (OPMs); Relaxation; Porous materials.

ABSTRACT

Optically pumped magnetometers (OPMs) based on alkali-atom vapors are ultra-sensitive devices for dc and low-frequency ac magnetic measurements. Here, in combination with fast-field-cycling hardware, we demonstrate applicability of OPMs in quantifying nuclear magnetic relaxation phenomena. Relaxation rate dispersion across the nT to mT field range enables quantitative investigation of extremely slow molecular motion correlations in the liquid state, with time constants >1 ms, and insight into the corresponding relaxation mechanisms. The 10-20 fT/ $\sqrt{\text{Hz}}$ sensitivity of an OPM between 10 Hz and 5.5 kHz ^1H Larmor frequency suffices to detect NMR signals from ~ 2 mL bulk liquid, or 0.5 mL liquid imbibed in simple mesoporous materials, following nuclear spin prepolarization adjacent to the OPM. The expected limits of the OPM technique are discussed regarding measurement of relaxation rates above 100 s^{-1} .

INTRODUCTION

Nano-scale dynamic processes that occur on ms to μs time scales, such as protein folding, aqueous complexation and surface adsorption phenomena, are often probed using nuclear magnetic relaxation dispersion (NMRD) techniques¹⁻³, in which field-dependent relaxation rates of nuclear spins are used to infer correlation times for molecular reorientation^{4,5} and diffusive transport. Beyond fundamental interests, insights from NMRD such as surface fractal dimension and roughness provide models for industrial catalysis and petrology, where liquids are confined inside porous solids and molecular diffusion is restricted by surface geometry⁶ as well as adsorption⁷. Furthermore, if coupled with spectroscopic dispersion via chemical shifts or spin-spin couplings, the dynamics can

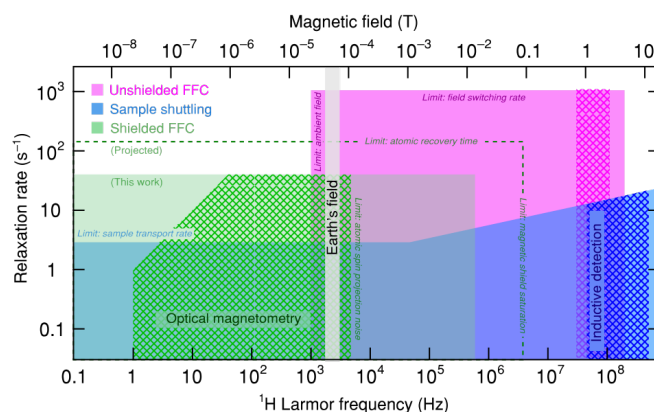


FIG. 1. Limits of existing NMRD techniques. Boundaries of the colored zones in the horizontal dimension indicate upper limits of longitudinal relaxation rate, $(T_{1,I}^{-1} \text{ s}^{-1})$, imposed by signal receiver dead time and/or speed of field-switching events. Boundaries in the vertical dimension indicate limits to the range of magnetic fields achievable by electromagnetic sources. Cross-hatching indicates Larmor frequencies where NMR signals are detected and corresponds to measurable transverse relaxation rates $T_{2,I}^{-1} \text{ (s}^{-1}\text{)}$. The diagonal of slope 1 corresponds to the spectroscopic resolution limit where rates of Larmor precession and transverse relaxation are equal: $B\gamma_I/(2\pi) = T_{2,I}^{-1} \sim T_{1,I}^{-1}$.

be related to specific molecular functional groups, facilitating analyses of chemical mixtures and biological specimens⁸.

Accurate correlation times τ_c can be obtained by measuring nuclear spin relaxation across a range of Larmor frequencies $B\gamma_I \ll \tau_c^{-1}$ to $B\gamma_I \gg \tau_c^{-1}$, where B is the field strength and γ_I is the nuclear gyromagnetic ratio. Extremely slow correlations thus require measurements at ultralow magnetic fields, below Earth's field, within shielded enclosures such as a MuMetal chamber. The main existing NMRD technique uses fast-field-cycling (FFC) electromagnets⁹⁻¹² of around 1 T for efficient inductive NMR signal detection, but these must be used unshielded with active cancellation of ambient fields to access below the geomagnetic field range^{13,14}. Alternatively, NMRD is performed by transporting samples between persistent high- and ultralow-field locations¹⁵⁻¹⁹, but relatively slow transport times limit the observable τ_c at the high end. The limits of these existing techniques are illustrated by the magenta- and blue-shaded regions, respectively, of Figure 1.

^{a)} Electronic mail: michael.taylor@icfo.eu

In this work, we introduce a third scenario to address the top-left portion of **Figure 1** that lies outside the reach of inductive NMR pickup. The speed of the FFC approach is combined with the low-frequency sensitivity of a spin-exchange-relaxation-free (SERF)^{20–27} optically pumped magnetometer (OPM) to perform sensitive NMRD at ¹H Larmor frequencies from 1 Hz to 10 kHz, corresponding to regions of **Figure 1** shaded in green. The high sensitivity of SERF OPMS of order $1 \text{ fT}/\sqrt{\text{Hz}}$ ^{28,29} at signal frequencies down to a few Hz, rivals the best Superconducting Quantum Interference Device (SQUID)^{30,31} and high-Q inductive-pickup magnetometers below Earth’s field^{32,33}, with the advantage of cryogen-free operation and simple tuning based on Hartmann-Hahn matching of the OPM and NMR spin ensembles. Moreover in the NMRD context, the OPM is compatible both with MuMetal shielding and relatively weak prepolarizing fields of order 10 mT. The magnetic fields for relaxation and detection are supplied accurately and precisely (within 1 nT) following a one-off calibration procedure and can be cycled in less than 1 ms, resulting in atomic-response-limited dead times. Based on this configuration, we obtain the full experimental frequency dependence for low-frequency motional correlations that cannot be probed by inductive field-cycling NMR procedures. We perform a detailed characterization of the techniques using paramagnetic impurities in ¹H₂O. A system of *n*-octane (*n*-C₈H₁₈) and *n*-decane (*n*-C₁₀H₂₂) molecules absorbed upon porous alumina and titania in nanoscale confinement is then used as an example relevant to research in catalysis. Results unambiguously support dynamics models involving molecular diffusion among paramagnetic sites on the pore surface.

Diffusion dynamics from NMRD

When it covers the appropriate range of fields and time-scales, the relaxation measured in NMRD can relate model parameters of interest to molecular motion, surface structure and molecule-surface interactions^{34–36}. A central quantity of interest is the time correlation function $g(\tau) = \langle x(t)x(t+\tau) \rangle / \langle x(t)x(t) \rangle$ of the molecular motion. This is related to observable relaxation by the quantity $j(\omega) = \int_0^\infty g(\tau) \cos(\omega\tau) d\tau$, i.e. the cosine transform of $g(\tau)$. Here we assume a simple but useful model where the local field is inhomogeneous, with a randomly oriented component of root-mean-square amplitude B_{rms} . The longitudinal relaxation rate is $[T_{1,I}(\omega_I)]^{-1} = \gamma_I^2 B_{\text{rms}}^2 j(\omega_I)$ under standard perturbation (i.e. Redfield³⁴) assumptions. In the ideal case of unrestricted diffusion, a single correlation time is found, where $g(\tau) \propto \exp[-(\tau/\tau_c)]$ and the spectral density is a Lorentzian: $j(\omega) = \tau_c / (1 + \omega^2 \tau_c^2)$, where τ_c is the characteristic diffusion time. Inverse-square power law behavior is thus expected for $T_{1,I}^{-1}$ vs. ω_I , for $\omega_I \gg \tau_c^{-1}$.

Scenarios of constrained Brownian motion³⁷ such as diffusion in pores may yield several concu-

rent dynamics modes. Fitting to a distribution of correlation times $p(\tau')$ may be more appropriate: $[T_{1,I}(\omega_I)]^{-1} = \gamma_I^2 \int_0^\infty B_{\text{rms}}^2 p(\tau_c) \tau_c / (1 + \omega_I^2 \tau_c^2) d\tau_c$ ^{38,39}, where $p(\tau_c)$ represents a probability distribution normalized to $\int_0^\infty p(\tau_c) d\tau_c = 1$. Kimmich and co-workers examine this approach to explain power-law relaxation behavior in porous glasses: $T_{1,I} \propto \omega_I^\xi$, where $0 < \xi < 2$ ^{40,41}. Surface-induced relaxation is attributed to “molecular reorientation mediated by translational displacement” (RMTD), where diffusion across a rugged pore surface modulates intra-molecular spin-spin dipolar couplings and $p(\tau_c)$ is linked to the surface fractal dimension. A breakdown of the power law at low frequencies ω_I indicates a maximum τ_c , which is connected to the longest distance a molecule can diffuse before leaving the surface phase or experiencing a different surface structure. The value should depend on the molecule, due to different diffusion coefficients, as well as the porous medium.

Moreover towards zero Larmor frequency, $T_{1,I}$ tends to a plateau defined by $[T_{1,I}(0)]^{-1} = \gamma_I^2 \int_0^\infty B_{\text{rms}}^2 p(\tau_c) \tau_c = \gamma_I^2 B_{\text{rms}}^2 \langle \tau_c \rangle$, where $\langle \tau_c \rangle$ is the mean correlation time³⁶. This and the above measures all require $T_{1,I}$ to be known for frequencies below $\tau_{c,\text{max}}^{-1}$, motivating ultra-low field measurement capability.

RESULTS

NMR detection with tunable optical magnetometer

Figure 2a shows the experimental setup for FFC NMR with OPM detection. A 2 mL vial containing the NMR sample sits within four coaxial solenoids (S1 – S4), which provide a *z*-oriented field. Liquid coolant flows around the sample chamber, with S1 moreover immersed in the flowing coolant, to maintain a sample temperature around 30 °C. The short S1 solenoid is used to produce fields up to 20 mT to polarize the nuclear spins in the sample, while S2 and S3 provide weaker fields for Larmor precession. Adjacent to this chamber is a heated glass cell containing ⁸⁷Rb vapor, with optical access along the *x* and *z* directions for optical probing and pumping of the spin angular momentum **S** of the alkali atoms, respectively. The probe beam is linearly polarized and slightly detuned from the ⁸⁷Rb D₁ transition, such that on passing through the cell along the *x* axis it is optically rotated by an angle proportional to the polarization S_x .

A magnetic field ($B_1 \cos \omega t, B_1 \sin \omega t, B_{z,S}$) in Cartesian coordinates is assumed to be seen by the atoms, as the sum of a constant bias field $B_{z,S}$ along the *z* axis and a rotating field B_1 in the *x*–*y* plane due to nuclear Larmor precession in the sample. The rotating field assumes precession of nuclear spin angular momentum **I** about the *z* axis with Cartesian components $I_x(t) = I_0 \cos(\omega_I t)$ and $I_y(t) = I_0 \sin(\omega_I t)$ and that the nuclei experience a field $B_{z,I} = \omega_I / \gamma_I$.

Within the SERF regime the dynamics of **S** are also adequately described by a polarization vector model

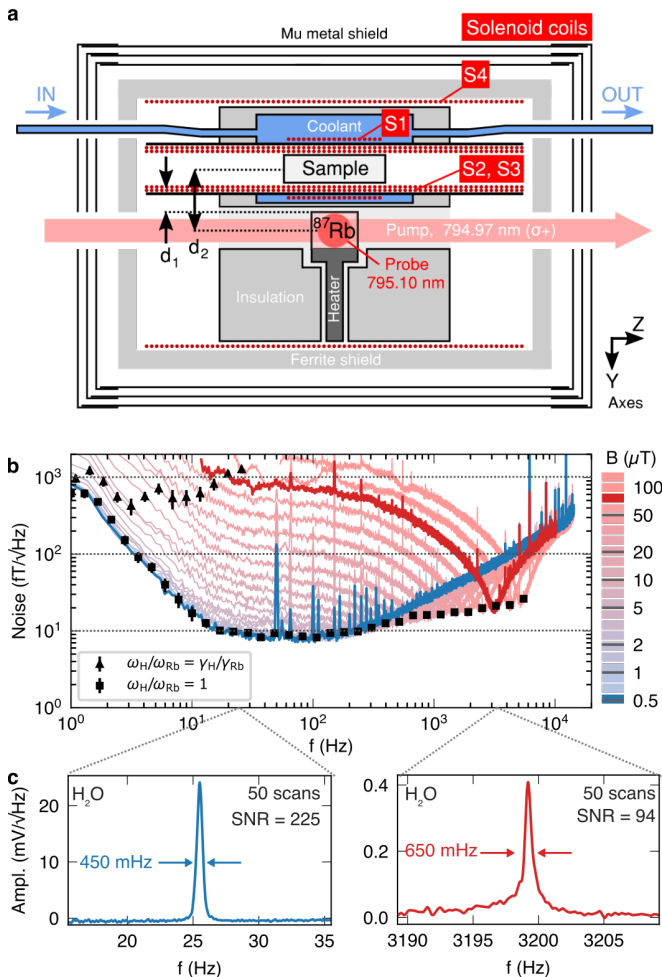


FIG. 2. Tunable NMR detection using an optically pumped magnetometer: (a) Schematic view of the apparatus through a vertical cross section. The MuMetal magnetic shield is cylindrically symmetric about the z axis. Standoff distance between sample container atomic vapor cell $d_1 = 3.5$ mm. Center-to-center distance between atomic cell and NMR sample $d_2 = 10$ mm; (b) Frequency dependence of magnetometer noise in field-equivalent units at magnetic bias fields $B_{z,I}$ ranging from 0.1 to 100 μ T. Plot markers indicate sensitivities at ^1H Larmor frequencies under the conditions of (■) tuned and (▲) untuned atomic Larmor frequencies; (c) Representative NMR signal and noise amplitudes in the tuned case for a sample of 1.8 mL milli-Q water, measured following pre-polarization at 20 mT and a transverse $\pi/2$ pulse.

where the x -axis component of \mathbf{S} under steady-state pump-probe and a transverse RF field of angular frequency ω is given by²⁹

$$S_x = \frac{g_S R_{\text{op}} T_{2,S}^2}{2q^2} \left[\frac{\cos \omega t + (\omega - \omega_S) T_{2,S} \sin \omega t}{1 + (\omega - \omega_S)^2 T_{2,S}^2} \right] B_1. \quad (1)$$

Here, $\omega_S = g_S B_{z,S}/q$ is the Larmor frequency, g_S is the gyromagnetic ratio, q is the nuclear slowing down factor, R_{op} is the optical pumping rate and $T_{2,S}^{-1}$ is the transverse relaxation rate of the alkali atom ensemble.

According to Equation 1 the atomic response to B_1 is strongest for equal precession frequencies of the spin species: $\omega_I = \omega_S$. Thus the OPM is tunable to a given NMR frequency by arranging the magnetic field at the atoms such that $B_{z,S} = \pm \gamma_I(q/g_S)B_{z,I}$. The apparatus permits this adjustment since $B_{z,I}$ is a superposition of the fields in the interior of coils S2 + S3 + S4, while $B_{z,S}$ is a superposition of the field from coil S4 and the much weaker exterior field of coils S2 + S3.

For Larmor frequencies $\omega_I/(2\pi)$ between 10 and 200 Hz the magnetometer noise is below 10 fT/ $\sqrt{\text{Hz}}$ (Figure 2b), limited by noise in the lasers and to a lesser extent the Johnson noise of the coils S1 + S2 + S3. The spin projection noise estimated from the atom density $n_S \approx 10^{20} \text{ m}^{-3}$, temperature 150 °C and coherence time $T_{2,S} \approx 3$ ms is $\sqrt{n_S g_S^2 T_{2,S}/q} \sim 1.1 \text{ fT}/\sqrt{\text{Hz}}$. Above fields $B_{z,S} \approx 100$ nT, ω_S starts to become comparable to $1/T_{2,S}$, marking the limit of the SERF regime, and the magnetometer noise rises above 20 fT/ $\sqrt{\text{Hz}}$. Overall, as Figure 2c illustrates, NMR signals are obtainable at fields where Larmor frequencies are around 100 times higher than the atomic bandwidth. In contrast, without tuning, the combined atomic and nuclear spin system yields a relatively narrow operating range for NMR, quantified by the half-width at half-height of Equation 1: $\Delta\omega_I/(2\pi) \approx g_S T_{2,S}/(2\pi q) \approx 80$ Hz.

Dissolved paramagnetic species in liquids

Nuclear magnetic relaxation due to molecular tumbling in simple, single-component liquids is normally characterized by an exponential correlation function with a time constant τ_c in the low ps range. Field-independent nuclear spin relaxation times are expected in the extreme-narrowing regime ($\omega_I \tau_c \ll 1$) below 10 MHz Larmor frequency and are experimentally observed.

Here ultralow-field NMR relaxation of ^1H spins is investigated for aqueous solutions of the paramagnetic compound 4-hydroxy-2,2,6,6-tetramethylpiperidin-1-oxyl (TEMPO). As shown in Figure 3a, we apply sequences A ($\pi/2$ pulse-acquire) and B (spin echo) after nuclear spin prepolarization at 20 mT. In A, prepolarization is followed by switching to a lower magnetic field during delay τ_1 , before a dc $\pi/2$ pulse induces NMR free nuclear precession about the z axis. The amplitudes s_A are fit well by the expected relation $s_A \propto \exp(-\tau_1/T_{1,I})$ (Figure 3b) and the observed relaxation rates scale linearly with concentration of the paramagnetic dopant as $T_{1,I}^{-1} = (T_{1,I}^{(0)})^{-1} + k_1[\text{TEMPO}]$, where $T_{1,I}^{(0)}$ is the relaxation time at zero solute (Figure 3c). The relaxivity parameter $k_1 = 0.453(5) \text{ s}^{-1} \text{ mmol}^{-1} \text{ dm}^3$ is in good agreement with literature values at the high-field end^{42,43}, which gives confidence in the method. Moreover, k_1 is independent of B_I , even down to near zero field.

Transverse ($T_{2,I}^*$) decoherence rates are obtained from line widths in the Fourier-transform NMR spectra of the

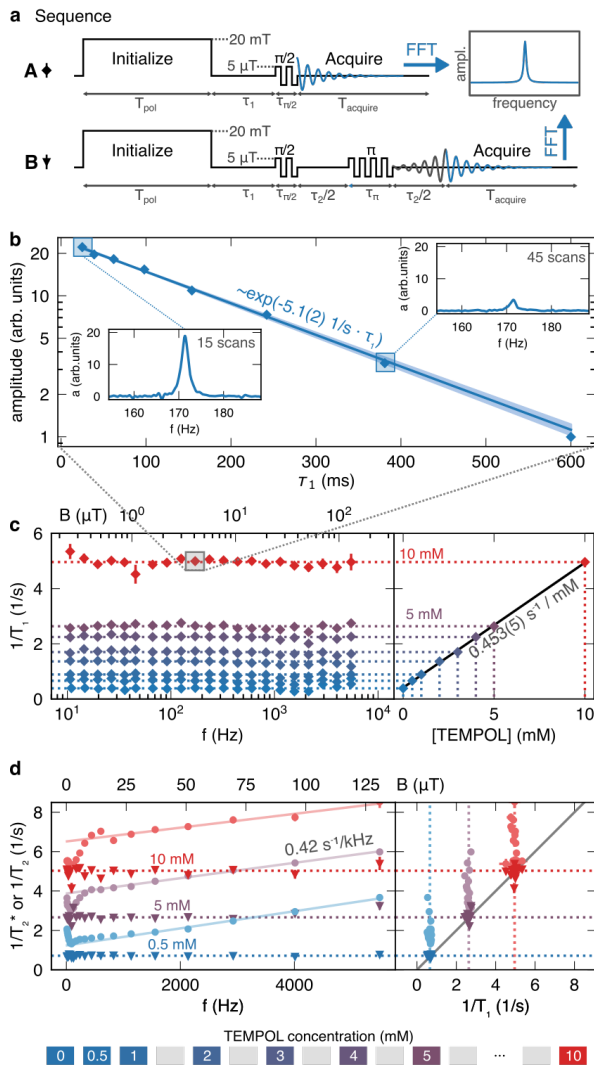


FIG. 3. NMR relaxation rates for spins $I = {}^1\text{H}$ in H_2O in aqueous TEMPOL solutions (30 ± 1 °C) are constant across the field range $25 \text{ nT} < B_{z,I} < 130 \mu\text{T}$: (a) Sequences A and B respectively measure longitudinal ($T_{1,I}^{-1}$; diamond plot markers) and transverse ($T_{2,I}^{-1}$ and $(T_{2,I}^*)^{-1}$; triangle and circle plot markers) relaxation rates. Vertical axis (not to scale) shows field strength with the polarization field along z and the $\pi/2$ and π pulses along y . Inset shows the Fourier-transform NMR precession signal; (b) Illustrative mono-exponential signal decay versus relaxation delay. Insets show corresponding NMR signals; (c) Field dependence of $T_{1,I}^{-1}$, which is independent of field $B_{z,I}$ but scales linearly with TEMPOL concentration; (d) Field dependence of $(T_{2,I}^*)^{-1}$ and $(T_{2,I})^{-1}$. $(T_{2,I}^*)^{-1}$ depends weakly on field due to instrument-specific gradients in $B_{z,I}$ and $B_{z,S}$, while $T_{2,I}^{-1}$ is approximately equal to $T_{1,I}^{-1}$.

sequence A data set and plotted in Figure 3d: $(T_{2,I}^*)^{-1} = \text{FWHM}/(2\pi)$. In contrast with longitudinal relaxation, rates $(T_{2,I}^*)^{-1}$ vary with Larmor frequency due to inhomogeneity in $B_{z,I}$. Firstly, S2+S3 produce a gradient with $dB_{z,I}/dz$ and smaller components along x and y due to tilt imperfections in the coil windings. The gradi-

ent is responsible for the linear slope $(d/dB_{z,I})(T_{2,I}^*)^{-1} = 0.01 \text{ s}^{-1} \mu\text{T}^{-1}$ (or 4 ppk of $B_{z,I}$) observed above 500 Hz Larmor frequency. We also note that coil S4 is centered on the OPM vapor cell, not on the NMR sample, and therefore gradients may cancel at certain Larmor frequencies; this effect is attributed to the line narrowing at around 200 Hz. The slope $(d/dB_{z,I})(T_{2,I}^*)^{-1}$ furthermore remains unchanged within error for a 0.10 mL volume of the solution and line widths do not improve even when compensation fields scaling as dB_x/dz , dB_y/dz , dB_z/dz are applied. Nevertheless, the decoherence introduced by gradients is small such that the NMR line width stays below 1 Hz even well above typical geomagnetic fields.

Transverse relaxation rates $T_{2,I}^{-1}$ free from gradient contamination are measured via the Hahn-echo sequence B (see Figure 3d, triangle plot markers). Signal amplitudes are fit well by the expected function $\exp(-\tau_1/T_{1,I} - \tau_2/T_{2,I})$ and provide a transverse relaxivity parameter $k_2 = 0.455(12) \text{ s}^{-1} \text{ mmol}^{-1} \text{ dm}^{-3}$ defined by $T_{2,I}^{-1}(B_{z,I}, [\text{TEMPOL}]) = T_{2,I}^{-1}(B_{z,I}, 0) + k_2(B_{z,I})[\text{TEMPOL}]$. The result $k_2 = k_1$ is consistent with isotropic molecular tumbling in the fast motion limit and holds down to Larmor frequencies of a few Hz, indicating the absence of slower motional correlations.

Liquids confined in porous materials

To demonstrate new insight into molecular motion near pore surfaces we study the ${}^1\text{H}$ spin relaxation of n -alkane hydrocarbons confined within matrices of alumina (γ polymorph, 9 nm mean pore diameter) and titania (anatase polymorph, 7–10 nm mean pore diameter). These simple inorganic oxides in their mesoporous form possess catalytic features due to their high specific surface area, Lewis acidic sites and option of chemical treatments including metalization to activate the pore surface. Yet, owing to the frequency range of conventional NMRD techniques, there is limited understanding of how molecular dynamics and surface site properties relate to long- τ_c relaxation processes, even without surface functionalization¹⁰.

Figure 4a shows ${}^1\text{H}$ relaxation rates at 30 °C for imbibed n -alkanes, measured between 1 Hz and 5.5 kHz Larmor frequency using the sequence shown in Figure 4b. Due to excess noise in the magnetometer below 100 Hz (including mains electricity noise and $1/f$ noise, see Figure 4c), fast field switching between relaxation and detection events is the preferred measurement option to probe the lowest fields, where the NMR signal is always detected at frequency above 100 Hz. Above 100 Hz Larmor frequency, the noise floor is low enough to detect NMR signals at the relaxation field, without switching. The measurable NMR relaxation is limited in principle to rates $T_{1,I}^{-1} < R_{\text{op}}^{-1}$, where the latter is of order 300 s^{-1} . However, in practice, the limit is $T_{1,I}^{-1} < T_{2,S}^{-1}$ or around 100 s^{-1} as the result of dead time caused by the atomic

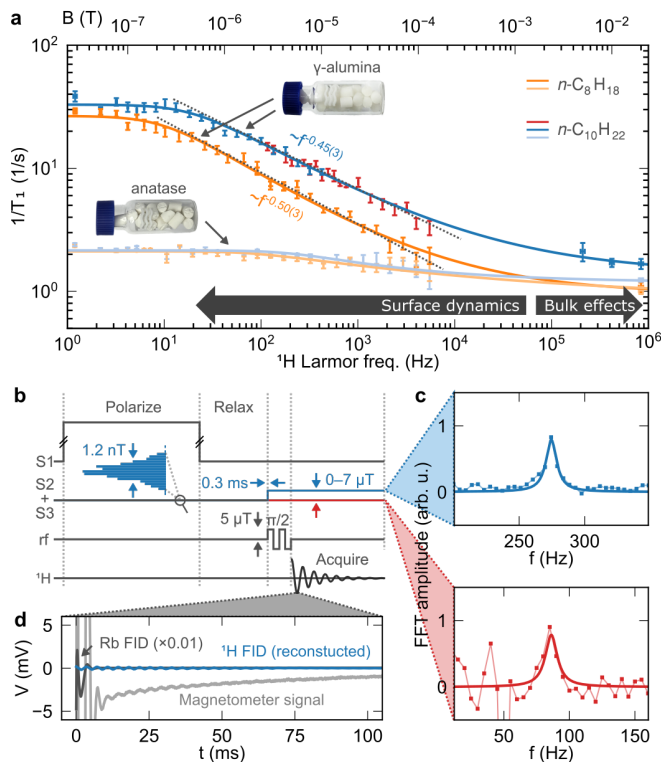


FIG. 4. (a) Longitudinal magnetization decay rates between Larmor frequencies 1 Hz and 5.5 kHz for n -octane and n -decane in porous γ -alumina and anatase titania. For n -decane in γ -alumina, colors indicate the NMR detection field, as discussed in the main text and represented in the rest of the figure. Data above 100 kHz correspond to magnetization buildup rates in the S1 field; (b) FFC pulse sequence used to measure $T_{1,I}$ decay at ultralow field; (c) frequency-domain and (d) time-domain NMR signal of n -decane in γ -alumina after relaxation at $\omega_I/(2\pi) = 85$ Hz. In (c), the NMR signal-to-noise ratios (snr) illustrate the FFC requirement below 100 Hz: poor snr at $\omega_I/(2\pi) = 85$ Hz is due to $1/f$ and 50 Hz noise of the OPM and transverse signal decay during the 10-20 ms receiver dead time in atomic response following magnetic field pulses; FFC switching to $\omega_I/(2\pi) = 275$ Hz between relaxation and detection events is optimal for high snr and short dead time. The reconstructed time-domain signal in (d) equates with the Lorentzian spectral line shape fitted in (c).

precession signal following the $\pi/2$ pulse (see Figure 4d).

The main feature of Figure 4a is the weak dispersion of $T_{1,I}^{-1}$ across the conventional FFC-NMR frequency range 10 kHz to 1 MHz¹⁰, for each alkane and moreover between the two porous materials. The relaxation rate for each alkane depends only slightly on the porous material, therefore bulk effects dominate the relaxation process in this frequency region. In contrast, longitudinal relaxation below 10 kHz depends strongly on the material and mechanisms related to the surface are prominent, with the highest relaxation rates being observed towards zero field. The $T_{1,I}$ dispersion in titania is much weaker than in γ -alumina; $T_{1,I}^{-1}$ reaches only around 2 s^{-1} be-

low 200 Hz, compared to 30 s^{-1} for alumina. Although the two materials have similar mean pore diameter and surface area/volume ratio, surface-induced relaxation is not so active in the first material. It is known from electron spin resonance spectroscopy⁴⁴ that the alumina contains a higher concentration of paramagnetic impurity – $[\text{Fe}^{3+}] \approx 2 \times 10^{16}\text{ g}^{-1}$ (i.e., ions per unit mass of the dry porous material) in alumina vs. $2 \times 10^{15}\text{ g}^{-1}$ in titania – suggesting that the lower-frequency relaxation mechanism involves dipole-dipole coupling between ^1H and the surface spins, rather than surface-induced modulation of intra-molecular ^1H - ^1H spin couplings.

Moreover, between $\omega_I/(2\pi) = 50$ Hz and 5000 Hz, the longitudinal relaxation in γ -alumina obeys a power-law frequency dependence: $T_{1,I} \propto \omega_I^\xi$. Fitted slopes $-d(\log T_{1,I}^{-1})/d(\log \omega_I)$ give exponents $\xi = 0.50 \pm 0.03$ for octane and $\xi = 0.45 \pm 0.03$ for decane. Such values are consistent with simple numerical simulations in which imbibed molecules randomly walk within a dilute matrix of non-mobile spins – such as surface paramagnets – where the strength of dipole-dipole interactions between the two spin species scales with the inverse cube of their instantaneous separation³⁸. This nonlinear dependence results in an example of Lévy walk statistics. A detailed characterization of these effects in the alumina system is ongoing work.

For a preliminary analysis the measured relaxation rates are fitted well by a stretched Lorentzian function $[T_{1,I,\text{fit}}(\omega_I)]^{-1} = [T_{1,I}(0)]^{-1}/(1 + \tau_c^2 \omega_I^2)^\beta + [T_{1,I}(\infty)]^{-1}$ with four independent fit parameters: $T_{1,I}(0)$, $T_{1,I}(\infty)$, τ_c and β . For $\omega_I \tau_c \gg 1$ and $T_{1,I,\text{fit}}(\omega) \ll T_{1,I}(\infty)$, the function is approximated by a power law with $\xi = 2\beta$. The fitted curves are plotted as solid lines in Figure 4a.

The parameter τ_c for alkanes in alumina is determined from the relaxation behavior below 50 Hz, where $T_{1,I}(\omega_I)$ changes from a power law frequency dependence to a constant, i.e., a plateau at $T_{1,I}(0)$. Using the analysis presented earlier, this indicates a maximum correlation time ($\tau_c = \tau_{c,\text{max}}$) of around 20-30 ms, which is at least two orders of magnitude longer than the maximum correlation time of more polar molecules in porous confinement, such as water. Relative to octane, the plateau for decane extends to a higher Larmor frequency, indicating a shorter $\tau_{c,\text{max}}$, despite octane having a higher self-diffusion coefficient as a bulk liquid. However, at this point τ_c is also of similar magnitude to the longitudinal relaxation time. Under such conditions the assumptions of standard NMR relaxation theories – such as the Wangsness-Bloch-Redfield theory – are not strictly justified as valid, in particular the coarse graining of time³⁴, where spin diffusion may be a part of the relaxation mechanism, or set an upper limit for the relaxation rate in the plateau. Whether this is true requires more information the physical process responsible for spin relaxation.

DISCUSSION AND OUTLOOK

The τ_c values obtained for alkanes in porous alumina are extremely long by FFC-NMR standards; comparable τ_c s are more commonly probed by pulsed-field gradient (PFG) diffusometry and rotating-frame ($T_{1\rho,I}$) relaxometry techniques⁴⁵. As the latter involve inductive signal detection at high magnetic field, data are susceptible to contamination by poor field homogeneity and radiofrequency offset errors, especially in heterogeneous samples with internal magnetic susceptibility gradients. In contrast, in ultralow-field FFC relaxometry, the magnetic fields are both accurately and precisely controlled, eliminating all concerns about magnetic field homogeneity. This is shown by the result $T_2 \sim T_1$. Moreover, for relaxation rates below 30 s^{-1} the Fourier-transform NMR spectrum line width is less than 10 Hz full width at half maximum. This is adequate to resolve many one and two-bond scalar spin couplings (e.g., ^{13}C - ^1H coupling) and therefore components of liquid mixtures, offering ultralow-field NMRD to probe other interplay between molecules and the pore, such as competitive adsorption.

Compared to high-field inductive-detected NMRD, ultralow-field OPM-detected NMRD still has some limitations. A main limitation, resulting from the Hartmann-Hahn matching condition, is that the OPM Faraday rotation signal contains free-precession responses of the sensor atom and NMR sample spins at the same frequency. The atomic response is at least two orders of magnitude stronger than the NMR signal and can easily saturate the digitizer, which leads to a “dead time” on the order of the optical pumping time (10 ms, see Figure 4d). Even when the digitizer is not saturated, the atomic response during this time is a nontrivial function of the preceding delays τ_1 and/or τ_2 , making $T_{1,I}$ difficult to estimate below ~ 20 ms. This currently forbids the application to chemical systems where molecules interact more strongly, namely liquids in nanopores (e.g. zeolites, shale) and interfaces with hydrogen bonding. In principle, switchable intensity control of the optical pumping beam⁴⁶ is a method to accelerate optical pumping after the magnetic field pulses and therefore reduce the dead time down to the field switching time, well below 1 ms, without compromising sensitivity; the pumping time scales inversely with optical power, while the atomic spin projection noise scales as the inverse square root.

Ultralow-field FFC NMRD may also in the future offer new study paths when enriched by nuclear spin hyperpolarization. As shown in Figure 2c only a few tens of scans result in $\text{snr} > 20$ dB, even though the spins are prepolarized to around 1 part in 10^8 at the 20 mT starting field. Nitroxide radical compounds such as TEMPOL are a source of higher electron spin polarization, around 1 part in 10^5 at 20 mT, that can be efficiently transferred to nuclei via the Overhauser effect at both high⁴² and ultralow⁴⁷ magnetic fields. Hyperpolarization via surface-supported paramagnetic species may also be an option. This may open the possibility of studying nuclear

polarization buildup near pore surfaces, which may provide different information from relaxation decay measurements. Persistent radicals are also used in preparations of strongly polarized nuclear systems for in-vivo magnetic resonance imaging, which enable clinically relevant, real-time observations of metabolism⁴⁸. These could profit from a knowledge of signal decay mechanisms at ultralow magnetic fields, either as an alternative source of image contrast or simply to minimize polarization losses before imaging/detection. In the present case, flat relaxation dispersion (see Figure 3b) shows that the relaxivity of aqueous TEMPOL remains constant across the range of magnetic fields 100 nT to 100 μT .

METHODS

A. Sample preparation

All samples studied in this work were contained in disposable glass vials (12 mm o.d., 20 mm length, 1.8 mL internal volume, 8-425 thread) sealed with a silicone septum and finger-tight polypropylene screw cap.

Preparation of TEMPOL samples: a 10 mM stock solution of the radical 4-hydroxy-2,2,6,6-tetramethylpiperidin-1-oxyl (Sigma Aldrich, CAS: 2226-96-2) was prepared in 5.0 mL deoxygenated milli-Q water and diluted to concentrations of 0.5, 1, 2, 3, 4, 5 and 10 mM with deoxygenated milli-Q water. The diluted solutions were not further de-gassed.

Preparation of porous materials samples: cylindrical extrudate pellets of meso-porous γ -alumina (Alfa Aesar product 43855, lot Y04D039: 3 mm diameter, 3 mm length, 9 nm BJH mean pore diameter, Langmuir surface area $250 \text{ m}^2 \text{ g}^{-1}$) and anatase titania (Alfa Aesar product 44429, lot Z05D026: 3 mm diameter, 4 mm length, 7–10 nm mean pore size, Langmuir surface area $150 \text{ m}^2 \text{ g}^{-1}$) were obtained commercially. Pellets were oven dried at 120°C for 12h to remove physisorbed H_2O and then imbibed in neat n-alkane for at least 12 h after recording the dry mass. Excess liquid on the pellet outer surface was gently removed using tissue paper. The pellets were then placed in a vial (see Figure 4a), sealed with the cap and the combined mass of pellet and imbibed hydrocarbon was recorded.

B. Optical magnetometer

The magnetometer employed to detect ^1H precession signals in the NMR samples operated as follows. A cuboid borosilicate glass cell of inner dimensions $5 \times 5 \times 8 \text{ mm}^3$ contained a droplet of rubidium-87 metal and 90 kPa N_2 buffer gas (Twinleaf LLC). The cell was electrically heated to a temperature of 150°C . A circularly polarized light beam along z axis (3 mW, tuned to the center of the collision-shifted D_1 wavelength) optically

pumped the atomic spin polarization to $S_z \approx 0.5$. Faraday rotation in a second, linearly polarized light beam (10 mW, 65 GHz red-shifted from the pump, along x axis) was used to non-resonantly probe the S_x component of atomic polarization, resulting in a sensitivity to the magnetic field component in the xy plane. The Faraday rotation was detected by polarimetry using a differential photodetector (Thorlabs PDB210A), which produced an analog voltage signal that was conditioned (amplified, filtered to eliminate high-frequency noise and dc offset) and digitized (60 ksps, 16-bit ± 5 V ADC range) before storage and further processing on a computer.

C. Magnetic coils

The vapor cell and heating assembly was placed as close as possible to the NMR sample vial at a standoff distance $d_1 = 3.5$ mm between outer walls of the vial and atomic vapor cell (see Figure 2a). In order of increasing distance away from the NMR sample, d_1 accounts for (i) S2 + S3 coil windings (34 AWG enameled copper wire, solenoid length 13 cm, diameter 14 mm), (ii) a carbon-fiber support structure, (iii) S1 coil windings (36 AWG enameled copper wire, solenoid length 2.5 cm, single layer), (iv) a water-cooling jacket (de-ionized water, flow rate 1 mLs^{-1}) to remove heat deposited when the polarizing coil is energized and to maintain a stable sample temperature, (v) a PEEK support structure and (vi) an air gap for further thermal insulation.

Field-to-current ratios inside each coil was calibrated using the frequency of ^1H precession frequency in a sample vial containing de-ionized water. These were S2: $7.59(3) \mu\text{T mA}^{-1}$; S3: $7.50(3) \mu\text{T mA}^{-1}$; S4: $150.1(5) \text{ nT mA}^{-1}$. The atomic spin precession frequency at the magnetometer vapor cell was used to calibrate the external field of coils S2: $-11.1(3) \text{ nT mA}^{-1}$; S3: $-4.4(2) \text{ nT mA}^{-1}$, or 1460 ppm and 580 ppm of the field at the vial, respectively.

D. Magnetic noise spectra

An ac test signal of ± 8 pT parallel with the y axis was applied to calibrate the Faraday response as a function of frequency and z bias field. The calibration vs. frequency was used to scale the spectral response of the balanced photodetector from units of $\text{V}/\sqrt{\text{Hz}}$ into $\text{T}/\sqrt{\text{Hz}}$. The maximum magnetic response at a given bias field was confirmed to equal the tuning condition where the atomic Larmor frequency matched the frequency of the ac signal, given the prior calibration of the magnetic field at the sample vial and magnetometer cell.

E. Field switching

Timing of the NMR pulse sequences and data acquisition was controlled by a microcontroller (Kinetis K20 series: time base 2 μs , precision 17 ns, CPU speed 120 MHz). Current to the polarizing coil was switched via a dual H-bridge circuit with parallel flyback diodes and the switching time was < 1.0 ms. Coils S2 and S4 were connected to a low-noise precision current source (Twinleaf model CSB-10, 20-bit resolution over ± 10 mA) with a low-pass LC filter in series, resulting in a combined switching and settling time of order 100 ms. The FFC solenoid coil S3 operated at a current < 1 mA direct from the microcontroller digital-to-analog converter (12-bit resolution, 0-1 mA) for rapid, precise field switching without feedback controls. Typical S3 switching times were 0.25 ms and the accuracy (determined from standard error in the mean NMR center frequency over repeated scans at $\omega_I/(2\pi) = 550$ Hz, see Figure 4b inset) was better than 1 nT. The residual interior field of the MuMetal shield (Twinleaf LLC, model MS-1F) along the x , y , and z axes of order 10 nT was also compensated for.

Under steady-state conditions with the pre-polarizing coil turned off, the cooling system maintained a temperature of 27–28 °C at a thermocouple attached to the outside wall of the sample vial. The steady-state temperature rose to 30–31 °C when the polarizing coil was energized at 20 mT (2.2 A).

ACKNOWLEDGMENTS

The work described is funded by: EU H2020 Marie Skłodowska-Curie Actions project ITN ZULF-NMR (Grant Agreement No. 766402); Spanish MINECO projects OCARINA (Grant No. PGC2018-097056-B-I00), the Severo Ochoa program (Grant No. SEV-2015-0522); Generalitat de Catalunya through the CERCA program; Agència de Gestió d'Ajuts Universitaris i de Recerca Grant No. 2017-SGR-1354; Secretaria d'Universitats i Recerca del Departament d'Empresa i Coneixement de la Generalitat de Catalunya, co-funded by the European Union Regional Development Fund within the ERDF Operational Program of Catalunya (project QuantumCat, ref. 001-P-001644); Fundació Privada Cellex; Fundació Mir-Puig; MCD Tayler acknowledges financial support through the Junior Leader Postdoctoral Fellowship Programme from “La Caixa” Banking Foundation (project LCF/BQ/PI19/11690021). The authors also thank Jordan Ward-Williams and Lynn Gladden (University of Cambridge) for providing samples of porous alumina and titania, and for discussions.

AUTHOR CONTRIBUTIONS

MCD Tayler proposed the study. S Bodenstedt prepared the samples, measured and analyzed the exper-

imental data and together with MCD Tayler built the experimental apparatus and made the theoretical interpretation. MCD Tayler wrote the manuscript with input from all authors. All authors reviewed the manuscript and suggested improvements. MCD Tayler and MW Mitchell supervised the overall research effort.

COMPETING INTERESTS

The authors declare no competing interests.

DATA AVAILABILITY

The data supporting the findings of this work are available from the corresponding author upon reasonable request.

REFERENCES

- Kimmich, R., Field Cycling in NMR Relaxation Spectroscopy Applications in Biological, Chemical and Polymer Physics, *Bull. Magn. Reson.* **1** (4), 195–218 (1979).
- Kimmich, R. (Ed.), *Field cycling NMR relaxometry: instrumentation, model theories and applications*, The Royal Society of Chemistry, Oxford (2018). ISBN 978-1-78801-154-9.
- Kimmich, R. and Anordo, E., Field-cycling NMR relaxometry, *Progr. Nucl. Magn. Reson. Spectrosc.* **44**, 257–320 (2004).
- Schneider, D. J. and Freed, J. H., Spin Relaxation and Motional Dynamics, *Advances in Chemical Physics* (eds. Hirschfelder, J.O., Wyatt, R.E. and Coalson, R.D.) John Wiley & Sons, Ltd., pp 387–527 (2007). ISBN 978-0-47014-122-9
- Deutch, J.M. and Oppenheim, I., Time Correlation Functions in Nuclear Magnetic Relaxation, *Adv. Opt. Magn. Reson.* **3**, 43–78 (1968).
- Bychuk, O. V. and O’Shaughnessy, B., Anomalous Diffusion at Liquid Surfaces, *Phys. Rev. Lett.* **74**, 1795–1798 (1995).
- Guo, J.-C. et al., Advances in low-field nuclear magnetic resonance (NMR) technologies applied for characterization of pore space inside rocks: a critical review, *Petr. Sci.* **17**, 1281–1297 (2020).
- Korb, J.-P., Multiscale nuclear magnetic relaxation dispersion of complex liquids in bulk and confinement, *Progr. Nucl. Magn. Reson. Spectrosc.* **104**, 12–55 (2018).
- Job, C., Zajicek, J. and Brown, M. F., Fast field-cycling nuclear magnetic resonance spectrometer, *Rev. Sci. Instrum.* **67**, 2113–2122 (1996)
- Ward-Williams, J., Korb, J.-P. and Gladden, L. F., Insights into Functionality-Specific Adsorption Dynamics and Stable Reaction Intermediates Using Fast Field Cycling NMR, *J. Phys. Chem. C* **122**, 20271–20278 (2018).
- Ferrante, G. and Sykora, S., Technical aspects of fast field cycling, *Adv. Inorg. Chem.*, **57**, 405–470 (2005).
- Anoardo, E., Galli, G. and Ferrante, G., Fast-field-cycling NMR: applications and instrumentation, *Appl. Magn. Reson.* **20**, 365–404 (2001).
- Anoardo, E. and Ferrante, G.M., Magnetic field compensation for field-cycling NMR Relaxometry in the ULF band, *Appl. Magn. Reson.* **24**, 85 (2003).
- Kresse, B., Privalov, A.F. and Fujara, F., NMR field-cycling at ultralow magnetic fields, *Solid State Nucl. Magn. Reson.* **40**, 1926–2040 (2011).
- Chou, C.-Y., Chu, M., Chang, C.F., Huang, T., A compact high-speed mechanical sample shuttle for field-dependent high-resolution solution NMR, *J. Magn. Reson.*, **214**, 302–308 (2012).
- Kaseman, D. C. et al., Design and implementation of a J-coupled spectrometer for multidimensional structure and relaxation detection at low magnetic fields, *Rev. Sci. Instrum.* **91**, 054103 (2020).
- Ganssle, P. J. et al., Ultra-low-field NMR relaxation and diffusion measurements using an optical magnetometer, *Angew. Chem. Int. Edn.* **53**, 9766–9770 (2014).
- Tayler, M. C.D., Ward-Williams, J. and Gladden, L.F., NMR relaxation in porous materials at zero and ultralow magnetic fields, *J. Magn. Reson.* **297**, 1–8 (2018).
- Zhukov I.V. et al., Field-cycling NMR experiments in an ultrawide magnetic field range: relaxation and coherent polarization transfer, *Phys. Chem. Chem. Phys.* **20**, 12396–12405 (2018).
- Savukov, I. M. and Romalis, M. V., NMR detection with an atomic magnetometer, *Phys. Rev. Lett.* **94**, 123001 (2005).
- Savukov, I. M., Seltzer, S. J. and Romalis, M. V., Detection of NMR signals with a radio-frequency atomic magnetometer, *J. Magn. Reson.* **185**, 214–220 (2007).
- Blanchard, J. W. and Budker, D., Zero- to ultralow-field NMR, *eMagRes* **5**, 1395–1409 (2016).
- Tayler, M.C.D. et al., Invited review article: Instrumentation for nuclear magnetic resonance in zero and ultralow magnetic fields, *Rev. Sci. Instrum.* **88**, 091101 (2017).
- Happer, W. and Tam, A. C., Effect of rapid spin exchange on the magnetic resonance spectrum of alkali vapors, *Phys. Rev. A*, **16**, 1877–1891 (1977).
- Savukov, I. M. and Romalis, M. V., Effects of spin-exchange collisions in a high-density alkali-metal vapor in low magnetic fields, *Phys. Rev. A* **71**, 023405 (2005).
- Allred, J. C., Lyman, R. N., Kornack, T. W. and Romalis, M. V., High-sensitivity atomic magnetometer unaffected by spin-exchange relaxation, *Phys. Rev. Lett.* **89**, 130801 (2002).
- Ledbetter, M. P., Savukov, I. M., Acosta, V. M., Budker, D. and Romalis, M. V., Spin-exchange-relaxation-free magnetometry with Cs vapor, *Phys. Rev. A*, **77**, 033408 (2008).
- Budker, D. and Romalis, M. V., Optical magnetometry, *Nat. Phys.* **3**, 227–234 (2007).
- Budker, D. and Jackson Kimball, D. F. (Eds.) *Optical Magnetometry*, Cambridge University Press (2013). ISBN 1107010357.
- McDermott, R., Trabesinger, A. H., Muck, M., Hahn, E., Pines, A. and Clarke, J., Liquid-state NMR and scalar couplings in micro-tesla magnetic fields, *Science* **295**, 2247–2249 (2002).
- Trahms, L. and Burghoff, M., NMR at very low fields, *Magn. Reson. Imag.* **28**, 1244–1250 (2010).
- Appelt, S., Kühn, H., Häsing, F. and Blümich, B., Chemical analysis by ultrahigh-resolution nuclear magnetic resonance in the Earth’s magnetic field, *Nature Phys.* **2**, 105–109 (2006).
- Suefke, M., Liebisch, A., Blümich, B. and Appelt, S., External high-quality-factor resonator tunes up nuclear magnetic resonance, *Nature Phys.* **11**, 767–771 (2015).
- Redfield, A.G., The theory of relaxation processes, *Adv. Magn. Opt. Reson.* **1**, 1–32 (1965).
- Kowalewski, J. and Maler, L., *Nuclear Spin Relaxation in Liquids*, Boca Raton: CRC Press (2018). ISBN: 9781351264600
- Halle, B., Jóhannesson, H., and Venu, K., Model-free analysis of stretched relaxation dispersions, *J. Magn. Reson.* **135**, 1–13 (1998).
- Klafter, J. and Schlesinger, M.F., On the relationship among three theories of relaxation in disordered systems, *Proc. Natl. Acad. Sci USA* **83**, 848–851 (1986).
- McDonald, P.J., and Faux, D.A., Nuclear-magnetic-resonance relaxation rates for fluid confined to closed, channel or planar pores, *Phys. Rev. E* **98**, 063110 (2018).
- Miyaguchi, T., Uneyama, T., and Akimoto, T., Brownian motion with alternately fluctuating diffusivity: stretched-exponential and power-law relaxation, *Phys. Rev. E* **100**, 012116 (2019).

- ⁴⁰Kimmich, R., Strange kinetics, porous materials and NMR, *Chem. Phys.* **284**, 253–285 (2002).
- ⁴¹Zavada, T. and Kimmich, R., Surface fractals probed by adsorbate spin-lattice relaxation dispersion, *Phys. Rev. E* **59**, 5848–5854 (1999).
- ⁴²Prandolini, M. J., Denysenkov, V. P., Gafurov, M., Endeward, B. and Prisner, T. F., High-Field Dynamic Nuclear Polarization in Aqueous Solutions, *Journal of the American Chemical Society*, **131**, 6090–6092 (2009).
- ⁴³Neugebauer, P. *et al.*, Liquid state DNP of water at 9.2 T: an experimental access to saturation, *Phys. Chem. Chem. Phys.* **15**, 6049–6056 (2013).
- ⁴⁴Ward-Williams, J. and Gladden, L.F., *personal communication*.
- ⁴⁵Price, W.S., *NMR studies of translational motion*, Cambridge University Press (2009). ISBN: 978-052180696-1.
- ⁴⁶Limes, M.E. *et al.*, Portable magnetometry for detection of biomagnetism in ambient environments, *Phys. Rev. Applied*, **14**, 011002 (2020).
- ⁴⁷Hilschenz, I. *et al.*, Dynamic nuclear polarisation of liquids at one microtesla using circularly polarised RF with application to millimetre resolution MRI, *J. Magn. Reson.* **305**, 138–145 (2019).
- ⁴⁸Sriram, R., Kurhanewicz, J. and Vigneron, D.B., Hyperpolarized carbon-13 MRI and MRS studies, *eMagRes* **3**, 311–324 (2014).